Journal of Alloys and Compounds 688 (2016) 14–21

Contents lists available at ScienceDirect

Journal of Alloys and Compounds

journal homepage: http://www.elsevier.com/locate/jalcom

Microstructural changes of Zr-based metallic glass during micro-electrical discharge machining and grinding by a sintered diamond tool

Hu Huang, Jiwang Yan*

Department of Mechanical Engineering, Keio University, Yokohama 223-8522, Japan

ARTICLE INFO

Article history:
Received 10 May 2016
Received in revised form
26 June 2016
Accepted 17 July 2016
Available online 19 July 2016

Keywords:
Metallic glass
Micro-electrical discharge machining
Grinding
Microstructural change
Crystallization
Sintered diamond

ABSTRACT

Micro-electrical discharge machining (micro-EDM) and grinding of Zr-based metallic glass (MG) were performed by using sintered polycrystalline diamond (PCD) as a hybrid tool. The microstructural changes of the workpiece surface layer were investigated. X-ray diffraction (XRD) patterns indicated that the ZrC phase and a few other unknown crystalline phases existed in the surface layer after micro-EDM. After shallow grinding, other new crystalline phases were detected on the surfaces. After deep grinding, however, the crystalline phases disappeared and an amorphous surface was obtained, the XRD and micro-Raman characteristics of which were similar to those of the as-cast MG surface. These results suggested that crystallization of MG in micro-EDM was hierarchical along the depth direction with different mechanisms. The results of surface morphology showed that grinding after micro-EDM not only effectively removed the crystallization layers to obtain an amorphous MG surface, but also improved the surface quality. The hybrid process provides a promising method to create three-dimensional micro features on a MG surface.

1. Introduction

Since their discovery in 1960, metallic glasses (MGs) without long-range topological order have attracted intensive and increasing attentions from multidisciplinary researchers because of their unique physical, chemical, and mechanical properties compared to their crystalline counterparts, such as high strength and hardness, large elastic limit and superior resistance to wear and corrosion [1–5]. However, due to the forming condition of MGs that requires high cooling rate, it is technologically difficult to prepare MGs with large size. Furthermore, MGs usually exhibit very limited macroscopic tensile plasticity followed by catastrophic failure, which also hinders their wide applications. Hence, currently, MGs are mainly applied in high-end products and high value-added components such as electronic frames, molds, precision surgical instruments, sport products, and micro-electro-mechanical devices [3]. In recent years, large amounts of studies involving in preparation, structure, mechanical properties as well as structure-property relationships of MGs have been carried out [5–13], and kinds of MGs with enhanced forming ability, increased size, and enhanced tensile plasticity have been developed.

In contrast, machinability of MGs has been given less attention, though it is undoubtedly very important from the perspective of application. Bakkal et al. [14–19] studied the machining characteristics of MGs during cutting and drilling, and found that although mechanical machining of MGs can obtain high dimensional accuracy and surface quality, some problems, such as oxidation and crystallization during high speed machining, still existed [14,20]. The severe tool wear because of the high hardness of MGs [15,16] and the formation of built-up edge due to the adhesion between the chip and tool in the contact region [21] affected the machining quality. Furthermore, for hard-brittle MGs [22] with hardness over 10 GPa but fracture toughness less that 10 MPa $m^{1/2}$, mechanical machining is more challenging. Alternatively, thermoplastic shaping in the supercooled temperature region provides a method for producing high value-added precision components [23–25], but some problems still exist [3,26], such as high cost and limited lifetime of molds. The crystallization of MGs during thermoplastic shaping because of hard-to-control forming temperature is another problem, especially for MGs with narrow supercooled temperature regions. Furthermore, the machining

* Corresponding author.
E-mail addresses: huanghu@keio.jp (H. Huang), yan@mech.keio.ac.jp (J. Yan).

http://dx.doi.org/10.1016/j.jallcom.2016.07.181
0925-8388/

flexibility by thermoplastic shaping is very low because the shape of components completely relies on the shape of molds. More suitable methods are greatly desired to machine MGs for their wider applications.

Recent research [27–29] indicated that as a nontraditional machining method, micro-electrical discharge machining (micro-EDM) can be used for flexible production of micro-parts and three dimensional structures such as micro-holes, micro-gears, micro-array, and micro-tools. Micro-EDM is also suitable for machining hard-brittle materials [29–31], and thus it has been widely used in die- and mold-making industry. In consideration of the limited size of MGs and their main applications in precision and micro-components, micro-EDM may be a good choice for machining MGs. However, micro-EDM is an electro-thermal process and MGs are very sensitive to temperature. The results obtained by Hsieh et al. [32] indicated that severe crystallization happened during the conventional EDM of Zr-based MG because of high electrical discharge energy. Our recent research [33] showed that the micro-EDMed surface of Zr-based MG retained better amorphous characteristics compared to the conventional EDM because of relatively low discharge energy.

The previous studies have revealed that crystallization of MGs occurs on the top surface in EDM. However, the microstructural changes of MGs in deeper subsurface region, i.e., heat affected zone during micro-EDM, have not been clarified. The penetration depth of the thermal damage into the bulk material is unknown. Moreover, for the purpose of maintaining the amorphous structure, the removal of the crystallization layers is undoubtedly very important. Up to date, however, there is no effective method to completely remove these layers.

In a recent study, we succeeded in completely removing the EDM-induced subsurface damage layer in single-crystal silicon carbide (SiC) by using sintered polycrystalline diamond (PCD) as a hybrid tool for micro-EDM and grinding [31]. If this method is also applicable to Zr-based MG, it may open an effective way to the high-quality fabrication of micro MG features and components. In the present study, the PCD hybrid tool was used to perform micro-EDM and grinding of Zr-based MG. The crystallization behaviors of Zr-based MG along the depth direction during micro-EDM will be investigated, and the depth of the crystallized layer will be estimated. Meanwhile, the complete removal of the crystallization layers by grinding using the same PCD tool will be attempted.

2. Materials and experiments

2.1. Materials

Disk-like MG samples with a diameter of 10 mm and thickness of 2 mm were cut from an as-cast $Zr_{41.2}Ti_{13.8}Cu_{12.5}Ni_{10}Be_{22.5}$ (commonly called Vitreloy 1) bar using a low speed diamond saw, and then, they were mechanically ground using 400, 800, and 1500 grit sand papers in sequence. This type of MG has been commercialized because of its high glass forming ability and wide supercooled liquid region [34], and it is a commonly used MG in scientific research. According to previous studies [35,36], the main thermophysical properties of Vitreloy 1 are summarized as glass transition temperature of 637 K, crystallization temperature of 733 K, liquidus temperature of 993 K, and thermal conductivity of 4 W/(m K).

2.2. Micro-EDM experiments

A precision micro-EDM machine (Panasonic MG-ED72, Japan) was used to implement micro-EDM of the MG. This machine has a Resistor-Capacitor (RC) discharge circuit and its stepping resolution in *xyz*-axes is 0.1 μm. Fig. 1(a) and (b) schematically show the material removal process during micro-EDM and subsequent grinding respectively. A sintered PCD rod with a diameter of 1 mm was selected as the machining tool both for micro-EDM and grinding. This PCD rod contains diamond grains with a mean size of 0.5 μm at a concentration of 90% in a Co binder, and its thermal conductivity is 290 W/(m K). Due to high thermal conductivity and high melting temperature, the wear of PCD tool during micro-EDM has been confirmed to be very low [37], which is beneficial to ensure the dimensional accuracy. Furthermore, during micro-EDM, diamond grains will be protruded out of the PCD tool surface by the electrical discharge dressing effect [31], which provides the opportunity to grind the micro-EDMed surface by the same tool as shown in Fig. 1(b) for studying and removing the crystallization layers because of the high hardness of PCD.

For each micro-EDM experiment, the same machining depth of 0.1 mm was set in the *z* direction. EDM oil, CASTY-LUBE EDS, was used as the dielectric fluid. The PCD electrode rotated with a constant speed of 3000 rpm, and meanwhile the MG sample moved in the *y* direction with a length of 1 mm by traverse feeding. Thus, micro-cavities were machined on the MG surface. The feed speed during micro-EDM was controlled automatically by the machine controller. For comparison, two voltages (70 V and 110 V) and capacitances (3300 pF and 1000 pF) were used during micro-EDM.

During grinding, the depth of cut in the *z* direction was 1 μm per tool pass, and the feed speed of the MG sample in the *y* direction was 25 μm/s. Three grinding depths, 10, 20, and 30 μm, were selected for comparatively analyzing the crystallization characteristics and surface quality.

2.3. Characterization

After micro-EDM and grinding, the samples were cleaned using acetone. Micro features of the machined surfaces were observed by a scanning electron microscope (SEM) (Inspect S50, FEI, USA). A color three dimensional (3D) laser scanning microscope (VK-9700, Keyence, Japan) was used to measure 3D topographies and surface roughness of the machined surfaces. Crystallization and carbonization of the machined surfaces were characterized by an X-ray diffractometer (XRD, D8 Discover, Bruker, Germany) and laser micro-Raman spectroscopy (NRS-3100, JASCO, Japan), respectively.

3. Results and discussion

3.1. Surface characteristics after micro-EDM

Fig. 2 presents the SEM morphologies of the micro-EDMed surfaces under various voltages and capacitances. Micro-cavities were generated on the MG surface as shown in Fig. 2(a), (c), and (e). Fig. 2(b), (d), and (f) are the local enlarged views at the center of the micro-cavities, showing the micro features in detail. For the same capacitance of 3300 pF, an increased voltage induced larger size of craters as shown in Fig. 2(b) and (d). For the same voltage of 110 V, a decreased capacitance also resulted in decreased crater size as shown in Fig. 2(d) and (f). This difference in crater size can be rationalized according to the difference of discharge energy, which is proportional to the capacitance and the square of voltage. High voltage and capacitance result in high discharge energy, which will improve the machining efficiency but induce larger size of craters as shown in Fig. 2(d). For the same machining depth of 0.1 mm, it took 63 min when the voltage and the capacitance were 70 V and 3300 pF respectively, while it only consumed 21 min when the voltage increased to 110 V. For the voltage of 110 V, when the capacitance decreased to 1000 pF, the machining time increased to 40 min again.

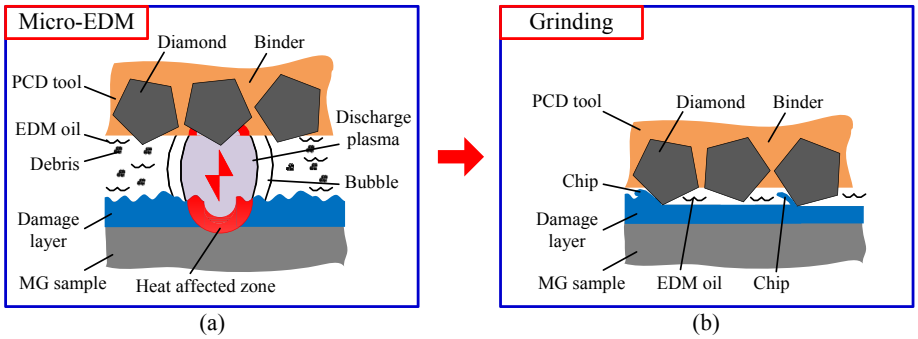

Fig. 1. Schematic diagrams of (a) micro-EDM and (b) grinding of Zr-based MG sample using PCD as a hybrid tool.

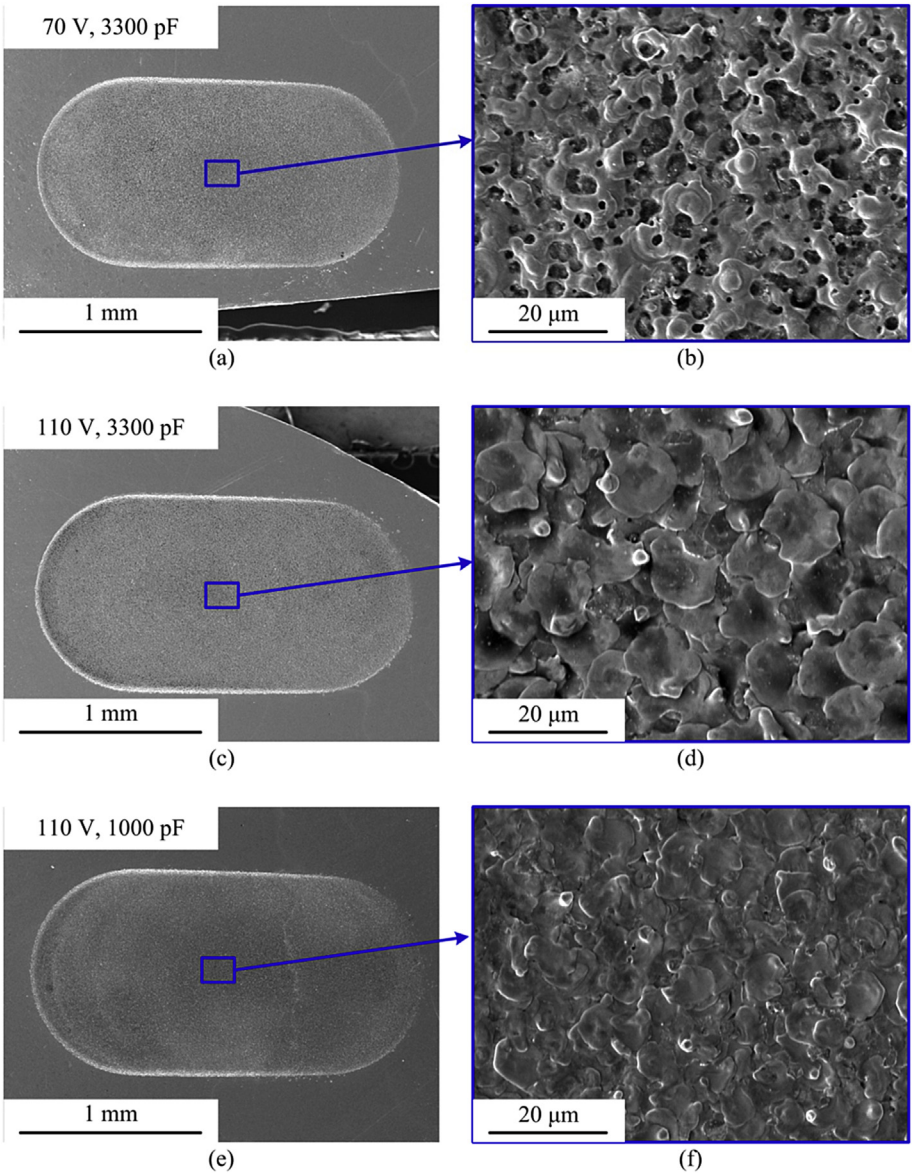

Fig. 2. SEM morphologies of the micro-EDMed surfaces under various voltages and capacitances: (a) and (b) 70 V, 3300 pF, (c) and (d) 110 V, 3300 pF, and (e) and (f) 110 V, 1000 pF.

Furthermore, Fig. 3 presents the 3D topographies and surface roughness of the micro-EDMed surfaces corresponding to the center regions of Fig. 2(a), (c), and (e). As shown in Fig. 3, the evaluated region is a rectangle with an area of 6656.360 μm^2, and the parameter R_a obtained by this instrument denotes the surface roughness of the total evaluated region. In Fig. 3(b) and (c), for the

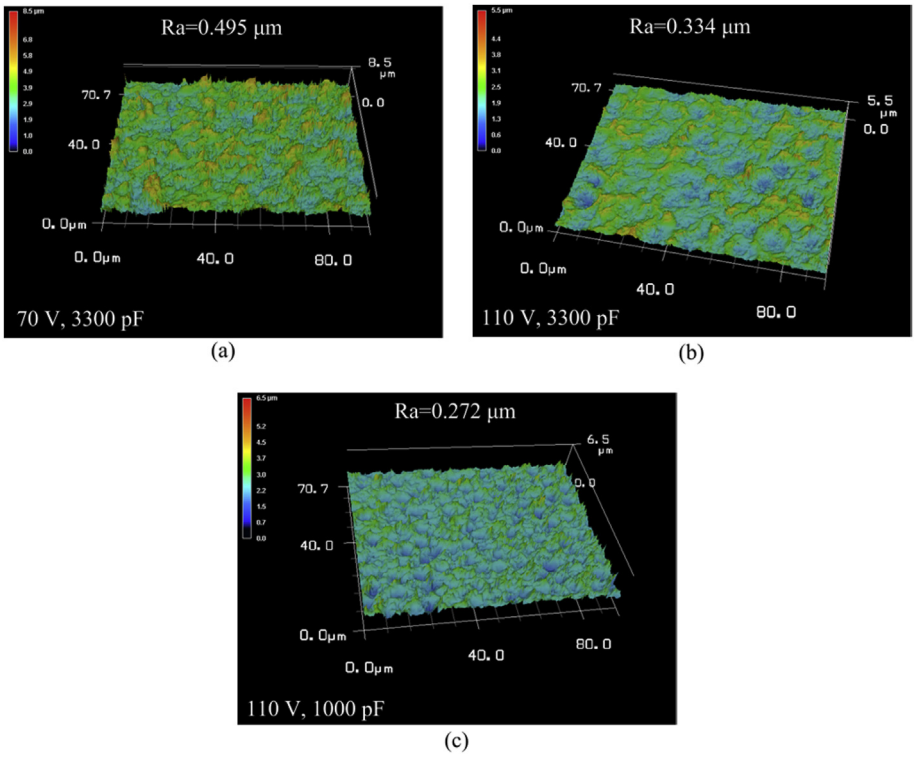

Fig. 3. 3D topographies and surface roughness of the micro-EDMed surfaces under various voltages and capacitances: (a) 70 V, 3300 pF, (b) 110 V, 3300 pF, and (c) 110 V, 1000 pF.

same voltage of 110 V, surface roughness decreased from 0.334 μm to 0.272 μm when the capacitance decreased from 3300 pF to 1000 pF, which can be explained by the decreased size of craters as shown in Fig. 2. However, for the same capacitance of 3300 pF, when the voltage decreased to 70 V, surface roughness did not decrease but increased to 0.495 μm. From Fig. 2(b), the increased surface roughness results from the formation of micro-voids, leading to discontinuity of the micro-EDMed surface. Thus, more bulges appear in Fig. 3(a), resulting in high surface roughness. While, for the voltage of 110 V, although the single crater is bigger, they overlapped with adjacent craters and few micro-voids were generated. Thus, relatively low surface roughness is obtained in Fig. 3(b).

Fig. 4 illustrates the XRD patterns of the micro-EDMed surfaces as well as the as-cast MG surface. A broad hump appears in the XRD pattern of the as-cast MG surface, demonstrating its amorphous nature. However, although the hump can still be identified in these XRD patterns obtained on the micro-EDMed surfaces, many sharp peaks are observed, suggesting remarkable crystallization in the top surface layer of the micro-EDMed surfaces. According to the XRD analysis software, sharp peaks at ~33.47°, 38.81°, 56.02°, 66.88°, and 70.29° denote the ZrC phase, and other peaks at ~83.28°, 92.77° and 95.98° are some unknown crystalline phases. In our previous research using a copper rod as the electrode [33], the micro-EDMed surfaces under the same experimental conditions retained better amorphous characteristics, showing very weak

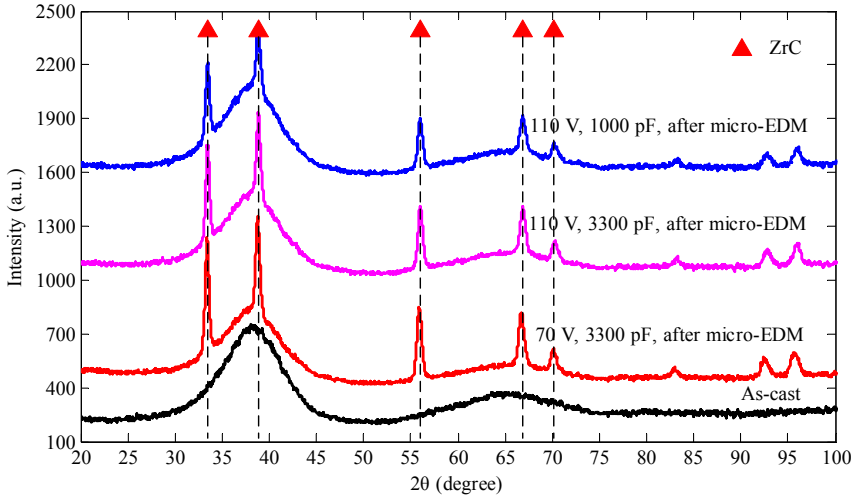

Fig. 4. XRD patterns of the as-cast MG surface and micro-EDMed surfaces under various voltages and capacitances.

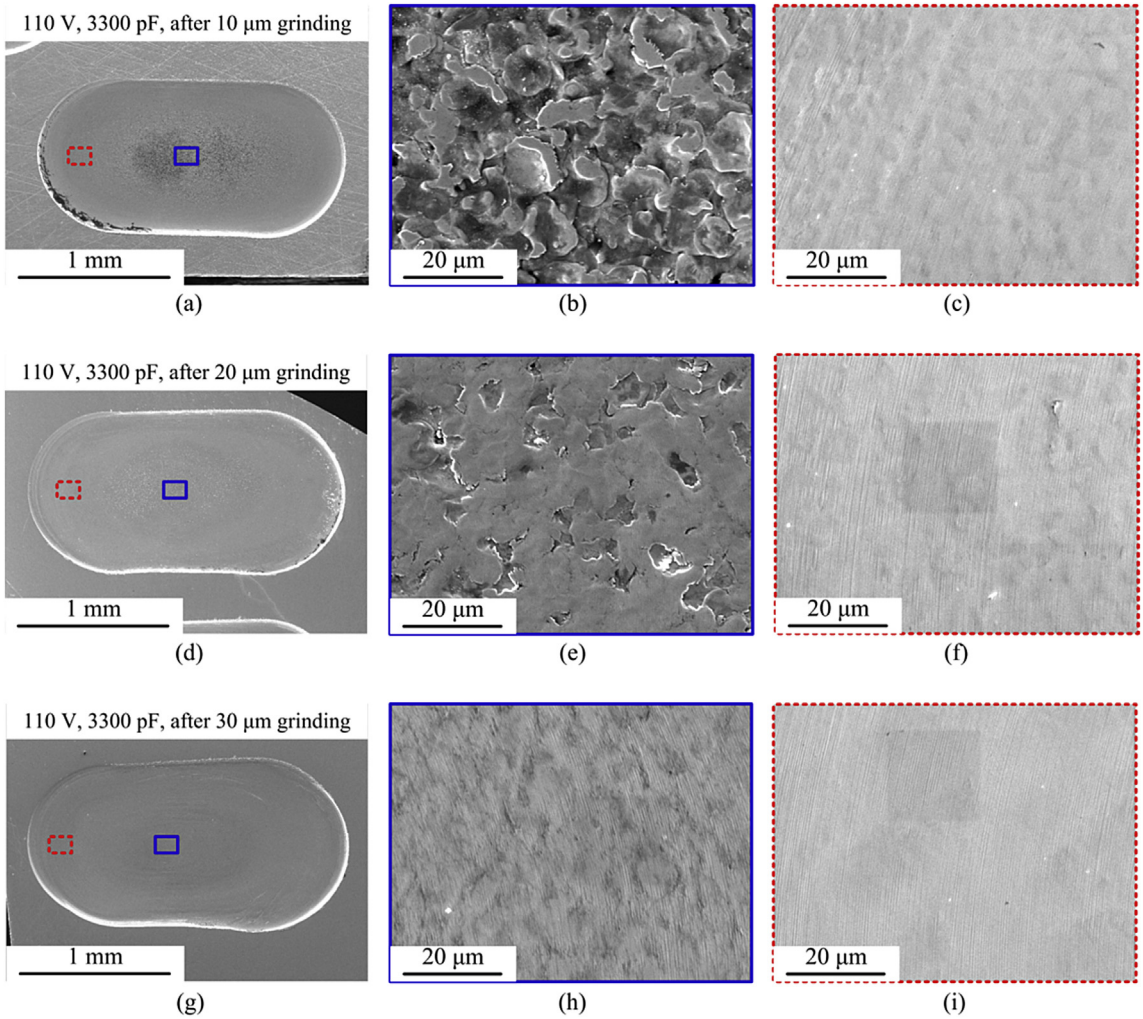

Fig. 5. SEM morphologies of the micro-cavities after grinding with various depths: (a)–(c) 10 μm grinding, (d)–(f) 20 μm grinding, and (g)–(i) 30 μm grinding. The voltage and capacitance during micro-EDM were 110 V and 3300 pF respectively. (b) and (c), (e) and (f), and (h) and (i) are local enlarged views of the solid and dashed rectangles in Figs. (a), (d), and (g) respectively, showing micro features of the center and side regions in detail.

crystallization peaks of ZrC. The enhanced crystallization peaks here indicated that surface crystallization was enhanced by using the PCD electrode. This results from the additional input source of carbon element from the decomposition of PCD, promoting the nucleation and growth of ZrC. This comparative analysis suggests that carbon-free electrodes such as copper are more suitable for micro-EDM of Zr-based MG because of retaining better amorphous characteristics. But the enhanced crystallization by using the PCD electrode benefits for studying crystallization behaviors along the depth direction in combination with subsequent grinding.

Furthermore, in Fig. 4, compared to the XRD patterns obtained under the voltage of 110 V and capacitance of 1000 pF, a slight increase of the intensity can be observed under the increased capacitance of 3300 pF and decreased voltage of 70 V, which results from the enlarged heat affected zone but lowered cooling rate at the increased capacitance, and increased thermal cycles and accumulation because of increased machining time at the decreased voltage, respectively. Overall, in Fig. 4, this difference in XRD intensity under current micro-EDM conditions is not conspicuous, indicating that crystallization of Vitreloy 1 MG during micro-EDM using the PCD electrode had low sensitivity to experimental conditions.

3.2. Surface characteristics after grinding

To study the crystallization behaviors along the depth direction as well as to remove the crystallization layer, grinding of the micro-cavities with various depths was performed after micro-EDM using the same PCD tool. For concision, results under the voltage of 110 V and capacitance of 3300 pF during micro-EDM will be presented and discussed because of the maximum discharge energy. Figs. 5 and 6 present the SEM morphologies and 3D topographies of the micro-cavities after grinding with various depths, respectively. In Figs. 5(a), (c), and 6(b), after 10 μm grinding, the side of the micro-cavity became smooth and the craters formed during micro-EDM as shown in Fig. 2(d) had been removed. The surface roughness in this region decreased to 0.037 μm. While, in the center as shown in Figs. 5(b) and 6(a), some flat surfaces had generated because of the grinding, but the craters can still be obviously observed. Compared to the micro-EDMed surface in Fig. 3(b), the surface roughness in the center after 10 μm grinding also decreased to 0.270 μm. Furthermore, in Figs. 5 and 6, with the increase of the grinding depth from 10 μm to 30 μm, both the center and the side regions of the micro-cavities became smoother and smoother. As shown in Fig. 6(e) and (f), after 30 μm grinding, the surface roughness in the center and side decreased to 0.043 μm and 0.021 μm respectively.

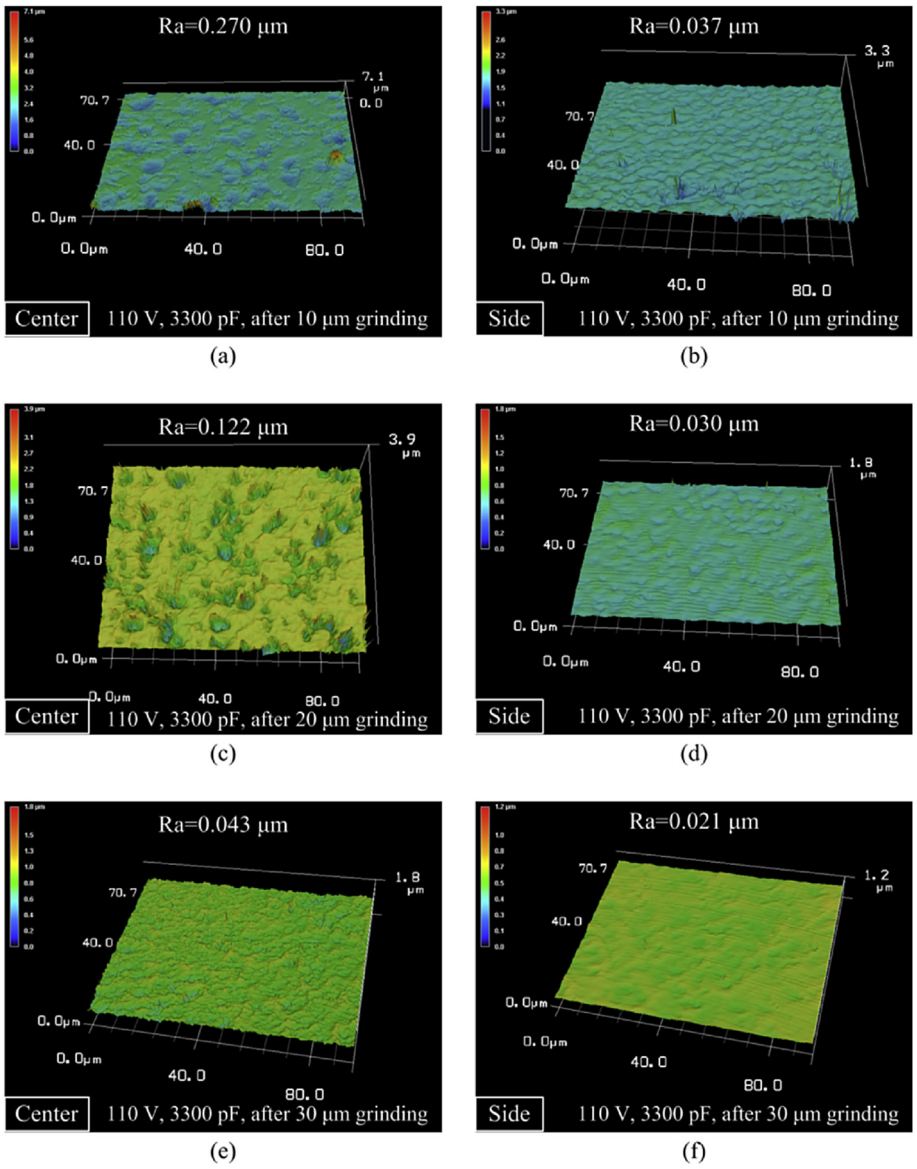

Fig. 6. 3D topographies and surface roughness of the micro-cavities after grinding with various depths, corresponding to those morphologies in Fig. 5. Detailed experimental conditions are inserted in each figure.

The difference in morphology and surface roughness in the center and side of the micro-cavity, results from the difference in real grinding depth. After micro-EDM, the machined surface was not flat [33]. The center region experienced more micro-EDM cycles compared to the side region, and more materials were removed during micro-EDM. Therefore, the center region was relatively lower than the side region. During grinding, the side region was firstly machined because of the relatively higher initial position. Hence, many grinding cycles had undergone in the side region before grinding could be performed in the center region, leading to formation of much smoother surface in the side region. So, the subsequent grinding not only reduced the surface roughness but also improved the surface flatness of the micro-cavities.

Fig. 7 illustrates the XRD patterns obtained on the surfaces of micro-cavities after grinding with various depths. For comparison, the XRD patterns obtained on the as-cast MG surface and the surface after micro-EDM are also presented. Interestingly, compared to the XRD pattern after micro-EDM, new sharp peaks at ~37.36°, 43.27°, 64.20°, 77.39°, and 98.22° appear on the XRD patterns after 10 μm and 20 μm grinding, demonstrating the existence of new crystalline phases in these depth layers. According to the XRD analysis software, the main new peaks at ~43.27° and 77.39° are close to the peaks of $CuTi_3$, and other peaks at ~37.36°, 64.20°, and 98.22° are not identified. Furthermore, the peaks of ZrC had been weakened in the XRD patterns after 10 μm and 20 μm grinding because of the partial removal of the top crystallization layer. Especially, in the XRD pattern after 30 μm grinding, nearly all the sharp peaks observed in the XRD patterns after micro-EDM, 10 μm and 20 μm grinding disappear both in the center and side regions of the micro-cavity, showing the XRD pattern similar to that of the as-cast MG surface. This means that the crystallization layers in both the top surface and the subsurface had been almost removed, and the amorphous MG exposed after 30 μm grinding. In Fig. 8, the surface after 30 μm grinding shows a similar micro-Raman spectrum to that of the as-cast MG surface, while remarkable peaks at ~1350 and 1580 cm^{-1} appear in the micro-Raman spectrum obtained on the surface after micro-EDM, denoting the formation of amorphous carbon [38]. Micro-Raman results in Fig. 8 further

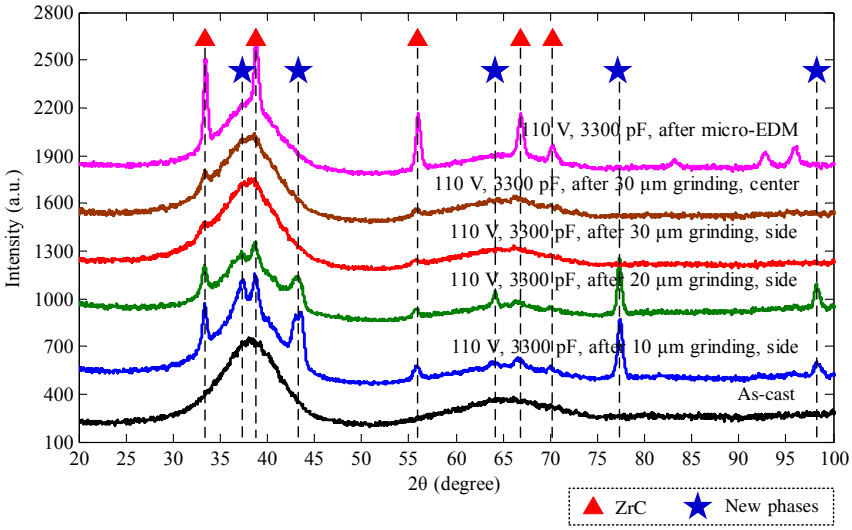

Fig. 7. XRD patterns obtained on the surfaces of the micro-cavities after grinding with various depths. For comparison, the XRD patterns obtained on the as-cast MG surface and the surface after micro-EDM are also presented.

confirm that grinding can effectively remove the crystallization and carbonization layers formed during micro-EDM. It should be noted that very weak peaks at ~33.47° and 56.02° can still be detected after 30 μm grinding in Fig. 7, but it is derived that with further increase of the grinding depth, a complete amorphous MG surface can be obtained. Because the machine used here is initially designed for micro-EDM, grinding with the depth over 30 μm was not performed to avoid damage of the machine.

The comparative results between the as-cast MG surface, the surface after micro-EDM, and the surfaces after grinding with various depths in Figs. 7 and 8 reveal a fact that crystallization of the micro-EDMed surface is hierarchical along the depth direction, which results from different thermal processes in the top surface and the subsurface during micro-EDM.

Micro-EDM involves in pulse-on and pulse-off processes. During the pulse-on time, sparks occur in the electrical discharge zone between the PCD electrode and MG sample, causing local heating, liquidizing, and vaporization of both the MG sample and PCD electrode. Meanwhile, sparks also induce decomposition of the EDM oil, generating decomposed carbon and hydrogen. Thus, liquidized and vaporized MG, decomposed carbon both from the PCD electrode and EDM oil, and other by-products from the PCD electrode and EDM oil such as molten and vaporized Co, co-exist in the electrical discharge zone. During the pulse-off time, because of high chemical affinity of Zr and C atoms, ZrC nucleates and grows accompanying with the cooling and re-solidifying process of liquidized and vaporized materials. Hence, ZrC phase can be detected in the top surface layer of the micro-EDMed surfaces as shown in Fig. 4. Compared to the case using the copper electrode in previous work [33], more carbon element existed in the EDM oil because of decomposition of the PCD electrode, which increased the possibility of ZrC nucleation and growth and further resulted in enhanced crystallization peaks of ZrC in Fig. 4. Those unknown peaks in Fig. 4 may result from the formation of some by-products by reaction with elements coming from decomposition of the PCD electrode. Because the hump remains in the XRD pattern after micro-EDM, crystalline phases had not grown sufficiently to occupy the entire top surface layer, and they were embedded in the amorphous matrix. In Fig. 2, some dark dots can be observed on the micro-EDMed surfaces. From Fig. 8, it can be derived that these dark dots result from the deposition of amorphous carbon. From the aforementioned analysis, crystallization of the top surface layer during micro-EDM mainly resulted from the formation of ZrC phase and some other unknown crystalline phases generated by reaction of MG elements with elements coming from the PCD electrode and EDM oil.

With regard to the appearance of new crystalline phases after 10 μm and 20 μm grinding, it results from the formation of internal crystalline phases in the amorphous matrix. These depth layers belong to the heat affected zone where the thermal process is significantly different from that of the electrical discharge zone. In the electrical discharge zone, each spark removes very tiny materials from the MG surface by heating, liquidizing, and vaporization, which is completed in a very short duration. Then, these tiny materials are cooled quickly by the surrounded flowing EDM oil. This fast heating and cooling process ensures that crystalline phases are hard to nucleate and grow between these elements of MG. However, in the heat affected zone, materials frequently experience heat cycles by thermal conduction from the upper electrical discharge zone, and heat is accumulated in this zone because of low thermal conductivity of MG. In certain depth layers, heat accumulation results in the local temperature over the crystallization temperature of Vitreloy 1, and thus crystalline phases nucleate and grow in these layers. The low thermal conductivity also lowers the cooling rate in

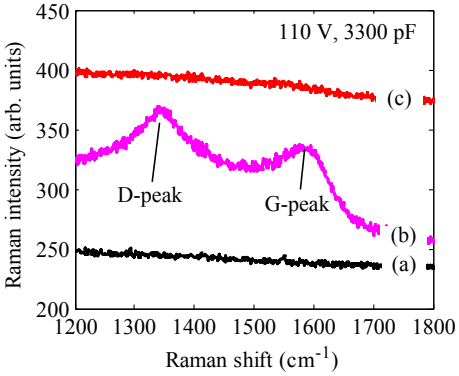

Fig. 8. Micro-Raman spectra of (a) the as-cast MG surface, (b) the surface after micro-EDM under the voltage of 110 V and capacitance of 3300 pF, and (c) the surface after 30 μm grinding.

these zones. These two factors contribute to the formation of crystalline phases inside the amorphous matrix. Accordingly, crystallization in these layers during micro-EDM for example 10 or 20 μm below the top surface layer mainly resulted from the formation of internal crystalline phases in the amorphous matrix because of the heat accumulation and low cooling rate.

These crystallization layers from the top surface to the subsurface region may lead to performance degradation of MGs. Results in this study indicate that subsequent grinding after micro-EDM can effectively remove these crystallization layers to obtain amorphous MG surface and meanwhile improve the surface quality. Hence, micro-EDM combined with subsequent grinding using the PCD as a hybrid tool is a promising method to machine micro features on the MG surface.

4. Conclusions

A PCD hybrid tool was used to perform micro-EDM and grinding of Zr-based MG. Crystallization behaviors of the MG along the depth direction during micro-EDM were investigated. Experimental results indicate that micro-EDM induced crystallization of the MG was hierarchical along the depth direction. In the top surface layer, crystallization mainly results from the formation of ZrC phase and some unknown crystalline phases generated by reaction of MG elements with elements coming from the PCD electrode and EDM oil during micro-EDM. Crystallization in the shallow subsurface region (~20 μm deep) mainly results from the formation of internal crystalline phases. The difference in crystallization behavior along the depth direction was rationalized by different thermal processes in the top surface layer and the subsurface region during micro-EDM. The subsequent grinding after micro-EDM can effectively remove the crystallization layers for achieving amorphous MG surface, and meanwhile, improving the surface quality. Micro-EDM combined with subsequent grinding using PCD as a hybrid tool is a promising method to machine micro features on MG surfaces.

Acknowledgement

Hu Huang is an International Research Fellow of the Japan Society for the Promotion of Science (JSPS) (ID No. is P 14048). This study has been financially supported by Grant-in-Aid for JSPS Fellows (Grant No. 26-04048). Authors also give thanks to Tsong Han Tan at Keio University for assistance in micro-EDM experiments.

References

[1] W.L. Johnson, Bulk amorphous metal – an emerging engineering material, JOM 54 (2002) 40–43.
[2] A.L. Greer, Metallic glasses, Science 267 (1995) 1947–1953.
[3] J. Plummer, W.L. Johnson, Is metallic glass poised to come of age? Nat. Mater. 14 (2015) 553–555.
[4] J. Schroers, Bulk metallic glasses, Phys. Today 66 (2013) 32–37.
[5] W.H. Wang, The elastic properties, elastic models and elastic perspectives of metallic glasses, Prog. Mater. Sci. 57 (2012), 487–656.
[6] J. Schroers, W.L. Johnson, Ductile bulk metallic glass, Phys. Rev. Lett. 93 (2004) 255506.
[7] W.H. Wang, C. Dong, C.H. Shek, Bulk metallic glasses, Mater. Sci. Eng. R 44 (2004) 45–89.
[8] H. Huang, J.L. Zhang, C.H. Shek, J.W. Yan, Effects of pre-compression deformation on nanoindentation response of Zr65Cu15Al10Ni10 bulk metallic glass, J. Alloy Compd. 674 (2016) 223–228.
[9] R. Maass, J.F. Loffler, Shear-band dynamics in metallic glasses, Adv. Funct. Mater. 25 (2015) 2353–2368.
[10] F.C. Li, J. Gu, M. Song, S. Ni, S.F. Guo, The evolution of local mechanical properties of bulk metallic glasses caused by structural inhomogeneity, J. Alloy Compd. 591 (2014) 315–319.
[11] F.C. Li, M. Song, S. Ni, S.F. Guo, X.Z. Liao, Correlation between hardness and shear banding of metallic glasses under nanoindentation, Mater. Sci. Eng. A Struct. 657 (2016) 38–42.
[12] R. Maass, K. Samwer, W. Arnold, C.A. Volkert, A single shear band in a metallic glass: local core and wide soft zone, Appl. Phys. Lett. 105 (2014) 171902.
[13] C. Su, Y. Chen, P. Yu, M. Song, W. Chen, S.F. Guo, Linking the thermal characteristics and mechanical properties of Fe-based bulk metallic glasses, J. Alloy Compd. 663 (2016) 867–871.
[14] M. Bakkal, A.J. Shih, S.B. McSpadden, C.T. Liu, R.O. Scattergood, Light emission, chip morphology, and burr formation in drilling the bulk metallic glass, Int. J. Mach. Tool. Manuf. 45 (2005) 741–752.
[15] M. Bakkal, A.J. Shih, S.B. McSpadden, R.O. Scattergood, Thrust force, torque, and tool wear in drilling the bulk metallic glass, Int. J. Mach. Tools Manuf. 45 (2005) 863–872.
[16] M. Bakkal, A.J. Shih, R.O. Scattergood, Chip formation, cutting forces, and tool wear in turning of Zr-based bulk metallic glass, Int. J. Mach. Tools Manuf. 44 (2004) 915–925.
[17] M. Bakkal, A.J. Shih, R.O. Scattergood, C.T. Liu, Machining of a Zr-Ti-Al-Cu-Ni metallic glass, Scr. Mater. 50 (2004) 583–588.
[18] K. Fujita, Y. Morishita, N. Nishiyama, H. Kimura, A. Inoue, Cutting characteristics of bulk metallic glass, Mater. Trans. 46 (2005) 2856–2863.
[19] D.X. Han, G. Wang, J. Li, K.C. Chan, S. To, F.F. Wu, Y.L. Gao, Q.J. Zhai, Cutting characteristics of Zr-based bulk metallic glass, J. Mater. Sci. Technol. 31 (2015) 153–158.
[20] M. Bakkal, C.T. Liu, T.R. Watkins, R.O. Scattergood, A.J. Shih, Oxidation and crystallization of Zr-based bulk metallic glass due to machining, Intermetallics 12 (2004) 195–204.
[21] H. Huang, H.W. Zhao, C.L. Shi, B.D. Wu, Z.Q. Fan, S.G. Wan, C.Y. Geng, Effect of residual chips on the material removal process of the bulk metallic glass studied by in situ scratch testing inside the scanning electron microscope, AIP Adv. 2 (2012) 042193.
[22] B.A. Sun, W.H. Wang, The fracture of bulk metallic glasses, Prog. Mater. Sci. 74 (2015) 211–307.
[23] J. Schroers, The superplastic forming of bulk metallic glasses, JOM 57 (2005) 35–39.
[24] W.L. Johnson, G. Kaltenboeck, M.D. Demetriou, J.P. Schramm, X. Liu, K. Samwer, C.P. Kim, D.C. Hofmann, Beating crystallization in glass-forming metals by millisecond heating and processing, Science 332 (2011) 828–833.
[25] J. Schroers, Processing of bulk metallic glass, Adv. Mater. 22 (2010) 1566–1597.
[26] G. Kaltenboeck, T. Harris, K. Sun, T. Tran, G. Chang, J.P. Schramm, M.D. Demetriou, W.L. Johnson, Accessing thermoplastic processing windows in metallic glasses using rapid capacitive discharge, Sci. Rep. U. K. 4 (2014) 6441.
[27] D. Wang, W.S. Zhao, L. Gu, X.M. Kang, A study on micro-hole machining of polycrystalline diamond by micro-electrical discharge machining, J. Mater. Process. Tech. 211 (2011) 3–11.
[28] J.W. Yan, T. Kaneko, K. Uchida, N. Yoshihara, T. Kuriyagawa, Fabricating microgrooves with varied cross-sections by electrodischarge machining, Int. J. Adv. Manuf. Tech. 50 (2010) 991–1002.
[29] J.W. Yan, K. Watanabe, T. Aoyama, Micro-electrical discharge machining of polycrystalline diamond using rotary cupronickel electrode, CIRP Ann. Manuf. Technol. 63 (2014) 209–212.
[30] Z.Y. Zhang, H.M. Peng, J.W. Yan, Micro-cutting characteristics of EDM fabricated high-precision polycrystalline diamond tools, Int. J. Mach. Tools Manuf. 65 (2013) 99–106.
[31] J.W. Yan, T.H. Tan, Sintered diamond as a hybrid EDM and grinding tool for the micromachining of single-crystal SiC, CIRP Ann. Manuf. Technol. 64 (2015) 221–224.
[32] S.F. Hsieh, S.L. Chen, M.H. Lin, S.F. Ou, W.T. Lin, M.S. Huang, Crystallization and carbonization of an electrical discharge machined Zr-based bulk metallic glass alloy, J. Mater. Res. 28 (2013) 3177–3184.
[33] H. Huang, J.W. Yan, On the surface characteristics of a Zr-based bulk metallic glass processed by microelectrical discharge machining, Appl. Surf. Sci. 355 (2015) 1306–1315.
[34] A. Peker, W.L. Johnson, A highly processable metallic-glass – Zr41.2Ti13.8-Cu12.5Ni10.0Be22.5, Appl. Phys. Lett. 63 (1993) 2342–2344.
[35] J.Z. Jiang, T.J. Zhou, H. Rasmussen, U. Kuhn, J. Eckert, C. Lathe, Crystallization in Zr41.2Ti13.8Cu12.5Ni10Be22.5 bulk metallic glass under pressure, Appl. Phys. Lett. 77 (2000) 3553–3555.
[36] C.C. Aydiner, E. Ustundag, M.B. Prime, A. Peker, Modeling and measurement of residual stresses in a bulk metallic glass plate, J. Non Cryst. Solids 316 (2003) 82–95.
[37] E. Uhlmann, M. Roehner, Investigations on reduction of tool electrode wear in micro-EDM using novel electrode materials, CIRP J. Manuf. Sci. Technol. 1 (2008) 92–96.
[38] E. Shibata, R. Sergiienko, H. Suwa, T. Nakamura, Synthesis of amorphous carbon particles by an electric arc in the ultrasonic cavitation field of liquid benzene, Carbon 42 (2004) 885–888.